ARTICLE

Nonlinear Electrical Impedance Tomography Method Using a Complete Electrode Model for the Characterization of Heterogeneous Domains

Jeongwoo Park, Bong-Gu Jung and Jun Won Kang[*]

Department of Civil and Environmental Engineering, Hongik University, Seoul, 04066, Korea

*Corresponding Author: Jun Won Kang. Email: jwkang@hongik.ac.kr

ABSTRACT

This paper presents an electrical impedance tomography (EIT) method using a partial-differential-equation-constrained optimization approach. The forward problem in the inversion framework is described by a complete electrode model (CEM), which seeks the electric potential within the domain and at surface electrodes considering the contact impedance between them. The finite element solution of the electric potential has been validated using a commercial code. The inverse medium problem for reconstructing the unknown electrical conductivity profile is formulated as an optimization problem constrained by the CEM. The method seeks the optimal solution of the domain's electrical conductivity to minimize a Lagrangian functional consisting of a least-squares objective functional and a regularization term. Enforcing the stationarity of the Lagrangian leads to state, adjoint, and control problems, which constitute the Karush-Kuhn-Tucker (KKT) first-order optimality conditions. Subsequently, the electrical conductivity profile of the domain is iteratively updated by solving the KKT conditions in the reduced space of the control variable. Numerical results show that the relative error of the measured and calculated electric potentials after the inversion is less than 1%, demonstrating the successful reconstruction of heterogeneous electrical conductivity profiles using the proposed EIT method. This method thus represents an application framework for nondestructive evaluation of structures and geotechnical site characterization.

KEYWORDS

Electrical impedance tomography; complete electrode model; inverse medium problem; Karush-Kuhn-Tucker (KKT) optimality conditions; nondestructive evaluation of structures

1 Introduction

Electrical impedance tomography (EIT) is a nondestructive evaluation method that infers the electrical conductivity, permittivity, or impedance of structures using the surficial measurement of electrical responses due to currents. The method seeks to construct a tomographic image of an object by estimating the spatial distribution of its impedance or electrical conductivity. EIT has been recognized as a highly applicable technique in medical imaging, industrial process monitoring, and near-surface site characterization due to its ease of field experimentation, economic feasibility, and superior ability to penetrate structures. When a structure experiences electric potential difference, current flows from the point of high potential to the point of low potential. In other words, when

the electric current is input to a structure, electric potential distribution is formed within the structure and on its boundary. If a structure is heterogeneous, the path of electric current is different from the homogeneous case. Therefore, the electric potential distribution of a structure depends on its material heterogeneity [1,2].

The problem of reconstructing the material properties of a structure using the measured electrical response from the surface can be defined as an inverse medium problem. Many mathematical algorithms and numerical strategies have been proposed to improve the solution to this problem. For example, mathematical and statistical regularization methods have been proposed to relieve the ill-posedness of the inverse problem and improve the solution convergence [3–6]. Representative methods for solving the nonlinear EIT problem include the back-projection method [7], one-step Newton method [8], D-bar method [9], and block method [10]. Recent studies have also investigated combining the EIT technique with neural networks to improve the accuracy of the tomographic image reconstruction of structures [11]. Such developments have been primarily applied to medical imaging for cancer detection and brain activity imaging. In civil engineering, research on the feasibility of applying the EIT to structural condition assessment or site characterization has been increasing recently. Recent applications of the EIT to civil structures include crack detection in pipes buried in the ground [12], ground saturation monitoring, and damage detection in carbon fiber-reinforced polymer (CFRP) materials [13]. To successfully implement the EIT, it is essential to have an efficient and accurate forward solver. In civil engineering applications, however, ensuring the accuracy of the forward solution remains a challenge because of the wide range of material properties, scales, and contact impedance between electrodes and structures.

For improving the previous development of the EIT for civil structures, this study proposes a nonlinear inversion method using a complete electrode model (CEM), targeting the reconstruction of the electrical conductivity profile of heterogeneous domains. The CEM comprises the Laplace equation for electric potential and the boundary conditions that express the current input to the structure via surface electrodes [14–16]. Because the CEM enables the realistic modeling of the interface between the structure and electrodes, accurate solutions of the electric potential in the structural medium and the electrodes are expected. The forward solution generated by the CEM is used within the nonlinear inversion framework for reconstructing the electrical conductivity profile of structures. Specifically, the inverse problem is resolved using a partial differential equation (PDE)-constrained optimization approach. This approach seeks the optimal solution of the medium's electrical conductivity to minimize a Lagrangian, which comprises a least-squares objective functional augmented by the weak imposition of the governing PDE and boundary conditions from the CEM. Enforcing the stationarity of the Lagrangian leads to state, adjoint, and control problems, which constitute the Karush-Kuhn-Tucker (KKT) optimality conditions. They are the first-order optimality conditions resulting from the first variation of the Lagrangian with respect to state, adjoint, and control variables. The electrical conductivity profile of the domain is then iteratively updated by solving the KKT conditions in the reduced space of the control variable. A conjugate gradient method with an inexact line search is used for the iterative solution of the electrical conductivity. To the best of the authors' knowledge, the EIT method based on the PDE-constrained optimization using the CEM and KKT conditions has been presented for the first time. The proposed inverse EIT problem deals with the Laplace equation, Robin, and Neumann boundary conditions in the PDE-constrained optimization. There are similar EIT approaches developed so far, but they mostly deal with Neumann or Dirichlet boundary conditions to solve the forward problem [17–19]. Some recent studies have included the Robin boundary condition to reflect the contact impedance between the domain and

electrode boundaries, but their inverse formulation and optimization schemes are different from the present study [20,21].

The remainder of this paper is organized as follows: In Section 2, the forward problem described by the CEM is presented. In Section 3, the formulation of the electrostatic inverse medium problem is presented using the Lagrangian functional and the first-order optimality conditions. In Section 4, the inversion process used to iteratively update the electrical conductivity profile in the reduced space is described. Section 5 discusses numerical examples for a series of cases in which homogeneous and heterogeneous electrical conductivity profiles are reconstructed. Finally, Section 6 presents the conclusions of the study. Finite differences for a non-unifrom grid are well shown in Figs. A1–A3.

2 Forward Problem

2.1 Problem Statement Using the Complete Electrode Model

To solve the inverse medium problem using measured electric potential values, it is first necessary to resolve the electrostatic forward problem for calculating the electric potential due to the current input. This study uses the CEM as a mathematical model for the forward problem. The CEM accounts for the current loss that occurs when the current flows to a low impedance material through an electrode and the voltage drops due to the contact impedance between the structural surface and electrode [14,22]. The current loss and voltage drop influence the measured electric potential values detected by the electrodes. As the CEM considers both the contact impedance and current loss at the electrodes, the error between the calculated electric potential and the experimentally derived electric potential is generally smaller than that computed using other models. Fig. 1 schematically shows a circular structure with electrodes on its surface. Solving the forward problem using the CEM reveals the electric potential inside the structure and that at the electrodes due to the current input through the electrodes.
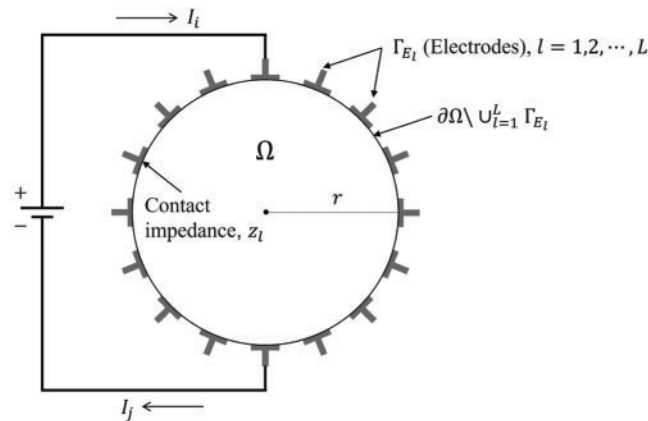
Figure 1: Schematic of a circular structure and surface electrodes

The forward problem described by the CEM can be formulated as the following boundary value problem:

$$\nabla \cdot (\sigma \nabla u) = 0, \quad \mathbf{x} \in \Omega, \tag{1}$$

$$u + z_l \sigma \frac{\partial u}{\partial n} = U_l, \quad l = 1, 2, \ldots, L, \quad \mathbf{x} \in \Gamma_{E_l}, \tag{2a}$$

$$\int_{\Gamma_{E_l}} \sigma \frac{\partial u}{\partial n} d\Gamma = I_l, \quad l = 1, 2, \ldots, L, \quad \mathbf{x} \in \Gamma_{E_l}, \tag{2b}$$

$$\sigma \frac{\partial u}{\partial n} = 0, \quad \mathbf{x} \in \partial\Omega \setminus \cup_{l=1}^{L} \Gamma_{E_l}, \tag{2c}$$

where Ω denotes the structural domain, u is the scalar electric potential, σ is the electrical conductivity, n is the outward unit normal on the boundary $\partial\Omega$, E_l denotes the lth electrode, Γ_{E_l} is the lth electrode boundary, z_l is the contact impedance of E_l, I_l is the injected current at E_l, U_l is the electric potential at E_l, and L is the number of electrodes. To ensure the existence and uniqueness of solutions, we add

$$\sum_{l=1}^{L} I_l = 0, \tag{3}$$

to the model. To determine the reference point for the electric potential,

$$\sum_{l=1}^{L} U_l = 0 \tag{4}$$

must be satisfied. We multiply Eq. (1) by a test function $v(\mathbf{x})$ and integrate it over the domain Ω, which results in

$$\int_{\partial\Omega} v\sigma \frac{\partial u}{\partial n} d\partial\Omega - \int_{\Omega} \nabla v \cdot (\sigma \nabla u) \, d\Omega = 0. \tag{5}$$

Using the boundary conditions (2a) and (2c), Eq. (5) can be rewritten as

$$\sum_{l=1}^{L} \frac{1}{z_l} \int_{\Gamma_{E_l}} v(U_l - u) d\Gamma - \int_{\Omega} \nabla v \cdot (\sigma \nabla u) \, d\Omega = 0. \tag{6}$$

Next, we integrate Eq. (2a) over Γ_{E_l}, which results in

$$\int_{\Gamma_{E_l}} u \, d\Gamma = \int_{\Gamma_{E_l}} \left(U_l - z_l \sigma \frac{\partial u}{\partial n} \right) d\Gamma = U_l |e_l| - z_l I_l. \tag{7}$$

Eq. (7) is multiplied by a test value V_l, divided by z_l, and summed for all electrodes, which yields

$$\sum_{l=1}^{L} \frac{1}{z_l} V_l \left(\int_{\Gamma_{E_l}} u \, d\Gamma - U_l |e_l| + z_l I_l \right) = 0. \tag{8}$$

Adding Eqs. (6) and (8) results in

$$\sum_{l=1}^{L} \frac{1}{z_l} \left[\int_{\Gamma_{E_l}} v(U_l - u) d\Gamma + V_l \left(\int_{\Gamma_{E_l}} (u - U_l) \, d\Gamma + z_l I_l \right) \right] - \int_{\Omega} \sigma \nabla v \cdot \nabla u \, d\Omega = 0,$$

$$\rightarrow \sum_{l=1}^{L} \frac{1}{z_l} \left[\int_{\Gamma_{E_l}} v(U_l - u) d\Gamma + V_l \left(\int_{\Gamma_{E_l}} (u - U_l) \, d\Gamma \right) \right] + \sum_{l=1}^{L} I_l V_l - \int_{\Omega} \sigma \nabla v \cdot \nabla u \, d\Omega = 0,$$

$$\rightarrow \int_{\Omega} \sigma \nabla u \cdot \nabla v \, d\Omega + \sum_{l=1}^{L} \frac{1}{z_l} \int_{\Gamma_{E_l}} (u - U_l)(v - V_l) \, d\Gamma = \sum_{l=1}^{L} I_l V_l. \tag{9}$$

Eq. (9) is the weak form of the forward problem. The electric potential u in the domain and the potential $\mathbf{U}$ at the electrodes are approximated using Legendre basis functions $\phi_i(\mathbf{x})$ and basis vectors $\mathbf{n}_j$, respectively:

$$u(\mathbf{x}) \cong u^h(\mathbf{x}) = \sum_{j=1}^{N} \alpha_j \phi_j(\mathbf{x}),$$ (10)

$$\mathbf{U} \cong \mathbf{U}^h = \sum_{j=1}^{L-1} \beta_j \mathbf{n}_j,$$ (11)

where N is the number of nodes in the finite element mesh. The coefficient α_j is the nodal value of $u(\mathbf{x})$, β_j is the unknown parameter for linearly combining vectors $\mathbf{n}_j$, and $\mathbf{U}^h$ is a vector consisting of the electric potential at each electrode. The basis vectors $\mathbf{n}_j \in R^{L \times 1}$ are defined as

$$\mathbf{n}_1 = \begin{bmatrix} 1 \\ -1 \\ 0 \\ 0 \\ \vdots \\ 0 \end{bmatrix}, \mathbf{n}_2 = \begin{bmatrix} 1 \\ 0 \\ -1 \\ 0 \\ \vdots \\ 0 \end{bmatrix}, \mathbf{n}_3 = \begin{bmatrix} 1 \\ 0 \\ 0 \\ -1 \\ \vdots \\ 0 \end{bmatrix}, \dots, \mathbf{n}_{L-1} = \begin{bmatrix} 1 \\ 0 \\ 0 \\ 0 \\ \vdots \\ -1 \end{bmatrix}.$$ (12)

The choice of $\mathbf{n}_j$ ensures that Eq. (4) is satisfied. The test function v and the value of V_l at the electrode can be similarly approximated as

$$v^h(\mathbf{x}) = \sum_{i=1}^{N} v_i \phi_i(\mathbf{x}),$$ (13)

$$\mathbf{V}^h = \sum_{i=1}^{L-1} V_i \mathbf{n}_i,$$ (14)

where $\mathbf{V}^h$ is a vector consisting of the value of V at each electrode. By substituting Eqs. (10), (11), (13), and (14) into the weak form represented by Eq. (9), a linear system of equations for unknown vector $\mathbf{u} = \begin{bmatrix} \boldsymbol{\alpha}^{\mathrm{T}} \boldsymbol{\beta}^{\mathrm{T}} \end{bmatrix}^{\mathrm{T}}$ can be obtained

$$\mathbf{Ku} = \mathbf{F}; \begin{bmatrix} \mathbf{B} & \mathbf{C} \\ \mathbf{C}^{\mathrm{T}} & \mathbf{D} \end{bmatrix} \begin{bmatrix} \boldsymbol{\alpha} \\ \boldsymbol{\beta} \end{bmatrix} = \begin{bmatrix} 0 \\ \mathbf{I} \end{bmatrix},$$ (15)

where the matrices and vectors are written as

$$B_{ij} = \int_{\Omega} \sigma \nabla \phi_i \cdot \nabla \phi_j d\Omega + \sum_{l=1}^{L} \frac{1}{z_l} \int_{\Gamma_{E_l}} \phi_i \phi_j d\Gamma \quad (1 \leq i \leq N) \quad (1 \leq j \leq N),$$ (16a)

$$C_{ij} = -\left(\frac{1}{z_1} \int_{\Gamma_{E_1}} \phi_i d\Gamma - \frac{1}{z_{j+1}} \int_{\Gamma_{E_{j+1}}} \phi_i d\Gamma \right) \quad (1 \leq i \leq N) \quad (1 \leq j \leq L-1),$$ (16b)

$$C_{ij}^{\mathrm{T}} = C_{ji} = -\left(\frac{1}{z_1} \int_{\Gamma_{E_1}} \phi_j d\Gamma - \frac{1}{z_{i+1}} \int_{\Gamma_{E_{i+1}}} \phi_j d\Gamma \right) \quad (1 \leq i \leq L-1) \quad (1 \leq j \leq N),$$ (16c)

$$D_{ij} = \begin{cases} \dfrac{|e_1|}{z_1}, & i \neq j \\ \dfrac{|e_1|}{z_1} - \dfrac{|e_{j+1}|}{z_{j+1}}, & i = j \end{cases} \quad (1 \leq i \leq L-1) \; (1 \leq j \leq L-1), \tag{16d}$$

$$\mathbf{0} \in R^{N \times 1}, \quad \mathbf{I} = \begin{bmatrix} I_1 - I_2 \\ I_1 - I_3 \\ I_1 - I_4 \\ \vdots \\ I_1 - I_L \end{bmatrix} \in R^{(L-1) \times 1}, \tag{17}$$

$$\boldsymbol{\alpha} = \begin{bmatrix} \alpha_1 \\ \alpha_2 \\ \alpha_3 \\ \vdots \\ \alpha_N \end{bmatrix} \in R^{N \times 1}, \quad \boldsymbol{\beta} = \begin{bmatrix} \beta_1 \\ \beta_2 \\ \beta_3 \\ \vdots \\ \beta_{L-1} \end{bmatrix} \in R^{(L-1) \times 1}. \tag{18}$$

In Eq. (16d), $|e_l|$ is the length of the lth electrode. Solving Eq. (15) yields nodal values of the electric potential in the domain as well as the values of β. The potentials U_l^h at the electrodes can be obtained as follows:

$$\mathbf{U}_l^h = \begin{bmatrix} U_1^h \\ U_2^h \\ U_3^h \\ \vdots \\ U_L^h \end{bmatrix} = \begin{bmatrix} \sum_{l=1}^{L-1} \beta_l \\ -\beta_1 \\ -\beta_2 \\ \vdots \\ -\beta_{L-1} \end{bmatrix}. \tag{19}$$

2.2 Validation of Forward Solutions

For validation, the forward solutions are compared to the solutions obtained using Technology Computer-Aided Design (TCAD) software. TCAD is used for modeling electronic design processes and the behavior of electrical devices based on fundamental physics [23]. Fig. 2 shows the configuration of a circular domain with a radius of 10 cm. The electrical conductivity of the domain is 1.56×10^{-1} S/cm. A total of 16 electrodes is arranged to cover 50% of the boundary; a current of 0.78 A is input into the fifth electrode, and it flows out through the 13th electrode. The contact impedance of the electrodes is 9.8×10^{-7} $\Omega \cdot$ cm². In this case, the potential of the fifth electrode is 10 V. Fig. 3 shows the distribution of the calculated electric potential within the domain due to the current input. The numerical solution calculated using the CEM is very close to the result obtained using the TCAD software.

(a) Homogeneous circular domain   (b) Finite element mesh
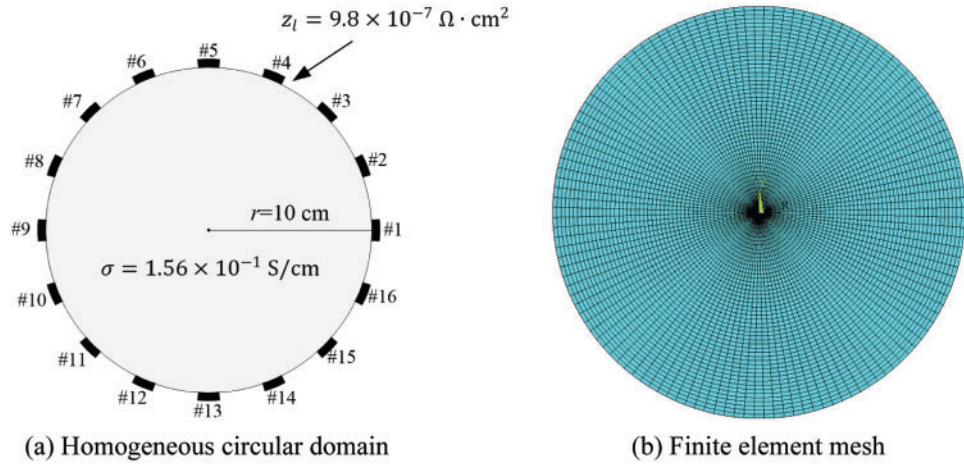
Figure 2: Homogeneous circular domain and finite element mesh for validating the forward solution

(a) $u(\mathbf{x})$ calculated by the CEM   (b) $u(\mathbf{x})$ calculated by the TCAD program
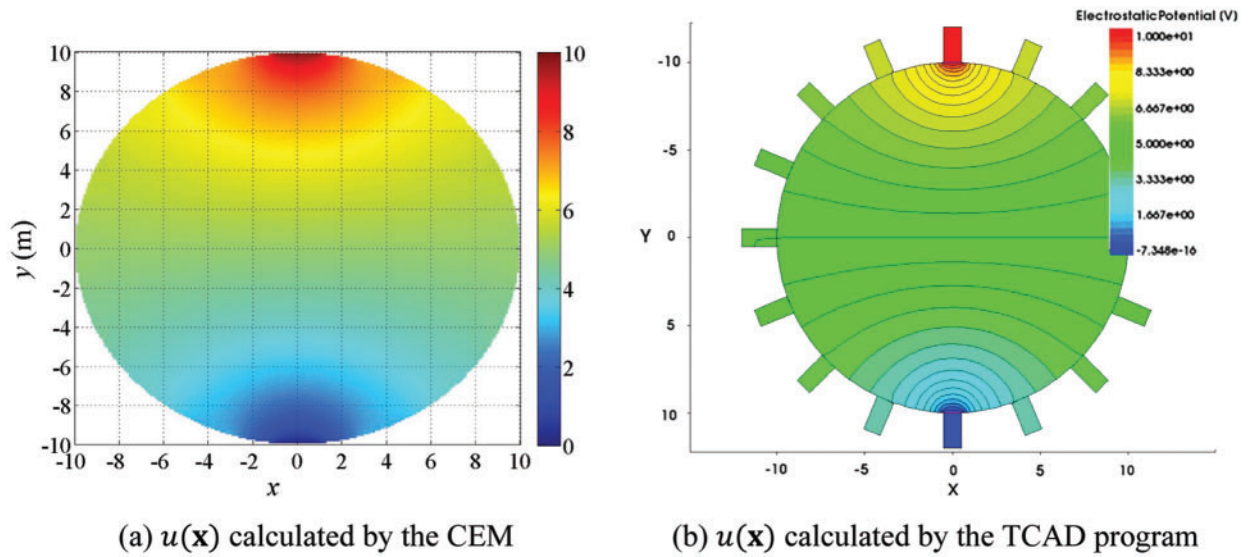
Figure 3: Calculated electric potential, $u(x)$, in the homogeneous circular domain

The error of the forward solution relative to the TCAD result can be calculated using the following equation:

$$\text{Error } (\%) = \frac{|V_{\text{CEM}} - V_{\text{TCAD}}|}{V_{\text{TCAD}}} \times 100. \tag{20}$$

Table 1 shows the electric potential values at each electrode and the corresponding relative errors. The maximum error is 3.37%, which demonstrates the accuracy of the forward solution. Fig. 4 depicts the electric potential, U_l, calculated at each electrode.

Table 1: Electric potential values at each electrode (calculated using the CEM and TCAD) and the corresponding relative errors

Position	CEM (V)	TCAD (V)	Error (%)
1	10.00	10.00	0.00
2	6.93	7.03	1.42
3	6.05	6.07	0.33
4	5.48	5.48	0.00
5	5.00	5.00	0.00
6	4.52	4.52	0.00
7	3.95	3.93	0.51
8	3.07	2.97	3.37
9	0.00	0.00	0.00
10	3.07	2.97	3.37
11	3.95	3.93	0.51
12	4.52	4.52	0.00
13	5.00	5.00	0.00
14	5.48	5.48	0.00
15	6.05	6.07	0.33
16	6.93	7.03	1.42
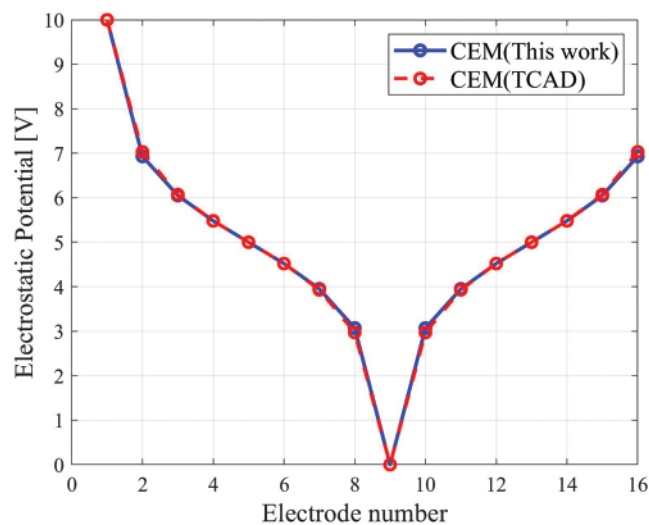
Figure 4: Graphical representation of the electrical potential at each electrode

2.3 Mesh-Type Dependency of the Forward Solution

For investigating the dependency of the forward solutions on the finite element mesh, two mesh types are explored: a radial mesh composed of eight-node quadrilateral elements and a mixed mesh with a square section inside. Fig. 5 illustrates these two types of meshes.

(a) Radial mesh   (b) Mixed mesh
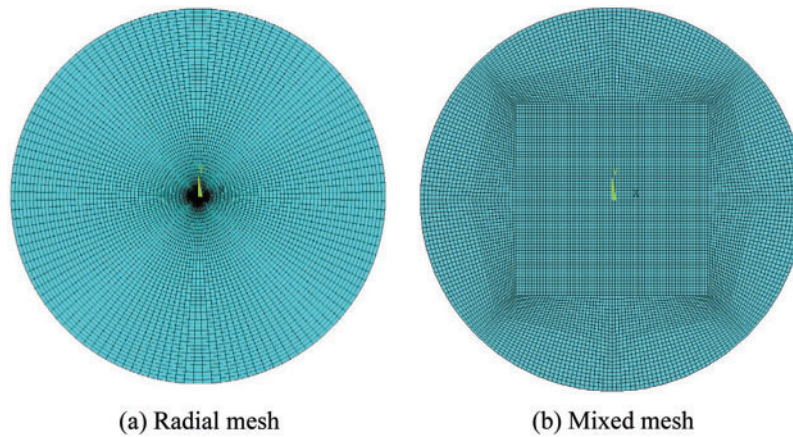
Figure 5: Two finite element mesh types for forward and inverse analyses

Fig. 6 shows a circular domain with a radius of 15 cm and electrodes attached to its boundary. The domain is assumed to be homogeneous, with an electrical conductivity of 1×10^{-2} S/cm, which is typical of concrete materials. A total of 32 electrodes is arranged on the boundary and are spaced evenly to cover 50% of the boundary (as for the domain described in Section 2.2). A current with a cosine pattern along the perimeter is input to each electrode. The magnitude of the current at each electrode is $I_l = \cos(2\pi l/L)$, where L is the total number of electrodes, and l is the index for the electrode number. The contact impedance of the electrodes is 0.22 $\Omega \cdot cm^2$. Fig. 7 presents the forward solutions calculated using the two meshes displayed in Fig. 5. Fig. 7c shows the calculated electric potential values at the electrodes on the boundary. The two results show that the forward solution changes minimally with the mesh type.
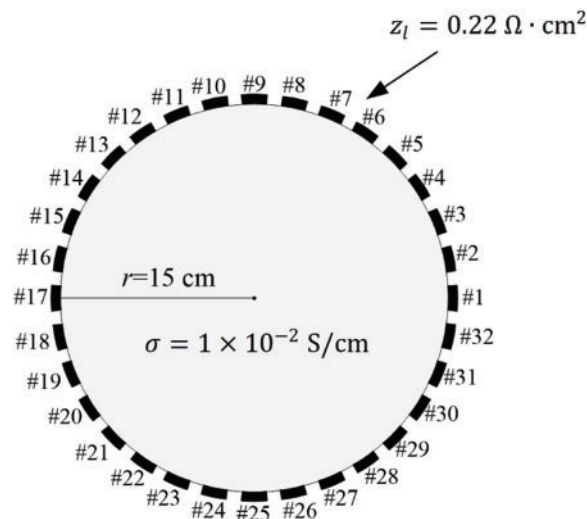
Figure 6: Homogeneous circular domain with 32 electrodes on the boundary

(a) $u(\mathbf{x})$ within the domain;
radial mesh

(b) $u(\mathbf{x})$ within the domain;
mixed mesh

(c) U_l at the lth electrode
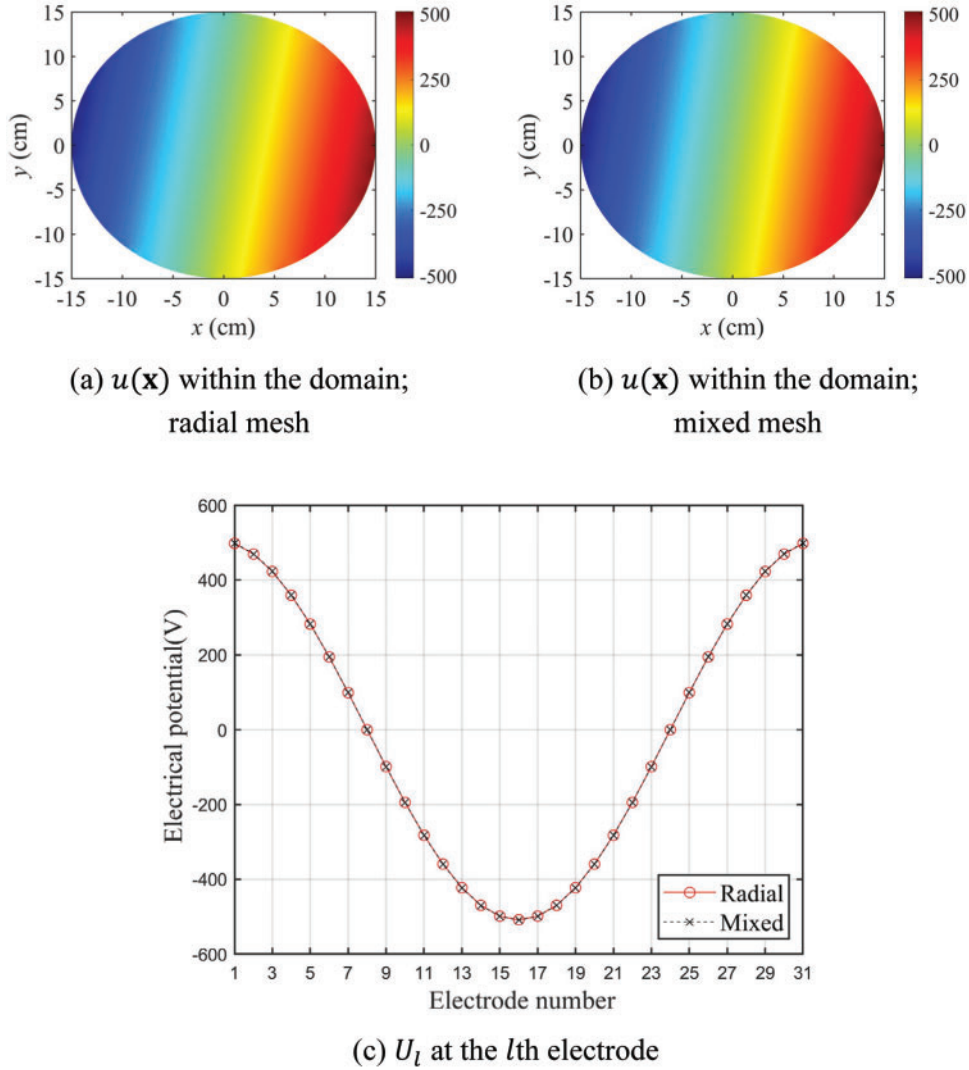
Figure 7: Forward solutions calculated using the two meshes

3 Inverse Problem

3.1 PDE-Constrained Optimization

The problem of reconstructing the electrical conductivity profile of a structure using the electric potential measured at surface electrodes can be formulated as the following PDE-constrained optimization problem:

$$\min_{\sigma(\mathbf{x})} J := \frac{1}{2} \sum_{l=1}^{L} \int_{\Gamma_{E_l}} \left(U_l - U_l^{\mathrm{m}}\right)^2 d\Gamma + \gamma(\sigma). \tag{21}$$

The objective functional J consists of a misfit functional in a least-squares sense and a regularization term $\gamma(\sigma)$. The misfit functional is expressed as the sum of the squared differences between the calculated electric potential U_l and the measured electric potential U_l^{m} at electrode E_l. This optimization problem is constrained by the governing Eq. (1) and boundary conditions (2)–(4) of the

forward problem. To relieve the ill-posedness of the inverse problem, the regularization term $\gamma(\sigma)$ is included in the objective functional J. In this study, the Tikhonov (TN) regularization scheme is used; thus, the regularization term can be written as

$$\gamma(\sigma) = \frac{1}{2} R_\sigma \int_\Omega \nabla\sigma \cdot \nabla\sigma \, d\Omega, \tag{22}$$

where R_σ is a regularization factor that controls the penalty to the gradient of the electrical conductivity $\sigma(\mathbf{x})$. Although TN regularization cannot accurately capture sharply varying material profiles, it still assists the inversion process in narrowing the feasibility space of solutions and improving the solution convergence.

3.2 First-Order Optimality Conditions

The PDE-constrained optimization problem can be converted to an unconstrained optimization problem using a Lagrange multiplier method. Specifically, the objective functional J can be augmented by Eqs. (1) and (2b) to construct the Lagrangian functional $\mathcal{L}$,

$$\mathcal{L}(u, U_l, w, W_l, \sigma) = \frac{1}{2}\sum_{l=1}^{L}\int_{\Gamma_{E_l}}\left(U_l - U_l^{\mathrm{m}}\right)^2 d\Gamma + \gamma(\sigma) + \int_\Omega w\nabla\cdot(\sigma\nabla u)\,d\Omega + \sum_{l=1}^{L}\int_{\Gamma_{E_l}} W_l\left(\sigma\frac{\partial u}{\partial n} - I_l\right) d\Gamma, \tag{23}$$

where w and W_l are Lagrange multipliers applied to the left-hand terms of the governing equation and boundary conditions, respectively. The electrical conductivity $\sigma(\mathbf{x})$ that minimizes the Lagrangian is the solution to the inverse problem. For the optimal solutions, first-order optimality conditions are introduced, which enforce the first variation of the Lagrangian with respect to state variables u and U_l, adjoint variables w and W_l, and the control variable σ to vanish.

3.2.1 First Optimality Condition: State Problem

At the optimum of the Lagrangian, its first variation with respect to the adjoint variables w and W_l should vanish. Introducing the stationarity conditions $\delta_w\mathcal{L} = 0$, $\delta_{W_l}\mathcal{L} = 0$, and $l = 1, 2, \ldots L$ results in the state problem, which is identical to the forward problem presented in Eqs. (1) and (2).

3.2.2 Second Optimality Condition: Adjoint Problem

At the optimum of the Lagrangian, its first variation with respect to the state variables u and U_l should vanish as well. Applying the stationarity requirements, $\delta_u\mathcal{L} = 0$, $\delta_{U_l}\mathcal{L} = 0$, and $l = 1, 2, \ldots L$, to the Lagrangian yields

$$\delta_u\mathcal{L} + \sum_{l=1}^{L}\delta_{U_l}\mathcal{L} = \sum_{l=1}^{L}\int_{\Gamma_l}\delta U_l\left(U_l - U_l^m - \sigma\frac{\partial w}{\partial n}\right) d\Gamma + \int_\Omega \delta u\nabla\cdot(\sigma\nabla w)\,d\Omega - \int_{\Gamma_f}\delta u\sigma\frac{\partial w}{\partial n}d\Gamma_f$$

$$+ \sum_{l=1}^{L}\int_{\Gamma_l}\frac{\partial\delta u}{\partial n}\sigma\left(w + z_l\sigma\frac{\partial w}{\partial n} + W_l\right) d\Gamma = 0. \tag{24}$$

Because δu and δU_l ($l = 1, 2, \ldots L$) are arbitrary, Eq. (24) results in the following adjoint problem:

$$\nabla\cdot(\sigma\nabla w) = 0, \quad \mathbf{x} \in \Omega, \tag{25}$$

$$w + z_l \sigma \frac{\partial w}{\partial n} = -W_l, \quad l = 1, 2, \ldots, L, \quad \mathbf{x} \in \Gamma_{E_l}, \tag{26a}$$

$$\sigma \frac{\partial w}{\partial n} = U_l - U_l^{\mathrm{m}}, \quad l = 1, 2, \ldots, L, \quad \mathbf{x} \in \Gamma_{E_l}, \tag{26b}$$

$$\sigma \frac{\partial w}{\partial n} = 0. \quad \mathbf{x} \in \partial\Omega \setminus \cup_{l=1}^{L} \Gamma_{E_l}, \tag{26c}$$

Eq. (25) is the governing equation for adjoint variable $w(\mathbf{x})$, and Eqs. (26a)–(26c) are boundary conditions for $w(\mathbf{x})$ and W_l. Eq. (26b) indicates the source of the adjoint problem, which depends on the potential misfit at the electrodes. The adjoint problem has the same differential operators as the state problem does.

3.2.3 Third Optimality Condition: Control Problem

Finally, the first variation of the Lagrangian with respect to the control variable σ should vanish at the optimum. Introducing the stationarity condition ($\delta_\sigma \mathcal{L} = 0$) to the Lagrangian results in

$$\delta_\sigma \mathcal{L} = R_\sigma \int_\Omega \delta\sigma \left(-R_\sigma \Delta\sigma - \nabla w \cdot \nabla u \right) d\Omega + \sum_{l=1}^{L} \int_{\Gamma_l} \delta\sigma \left(R_\sigma \frac{\partial \sigma}{\partial n} + w \frac{\partial u}{\partial n} + W_l \frac{\partial u}{\partial n} \right) d\Gamma$$

$$+ \int_{\Gamma_f} \delta\sigma \left(R_\sigma \frac{\partial \sigma}{\partial n} + w \frac{\partial u}{\partial n} \right) d\Gamma = 0. \tag{27}$$

Because $\delta\sigma$ is arbitary, Eq. (27) yields the following control problem:

$$- R_\sigma \Delta\sigma - \nabla w \cdot \nabla u = 0, \quad \mathbf{x} \in \Omega, \tag{28}$$

$$R_\sigma \frac{\partial \sigma}{\partial n} + w \frac{\partial u}{\partial n} + W_l \frac{\partial u}{\partial n} = 0, \quad l = 1, 2, \ldots, L, \quad \mathbf{x} \in \Gamma_{E_l}, \tag{29a}$$

$$R_\sigma \frac{\partial \sigma}{\partial n} + w \frac{\partial u}{\partial n} = 0. \quad \mathbf{x} \in \partial\Omega \setminus \cup_{l=1}^{L} \Gamma_{E_l} \tag{29b}$$

The control problem is a boundary value problem for the electrical conductivity $\sigma(\mathbf{x})$, with Eq. (28) being the governing equation and Eqs. (29a) and (29b) being the boundary conditions. The solution $\sigma(\mathbf{x})$ can be calculated once the state and adjoint solutions u, w, and W_l are obtained. The state, adjoint, and control problems constitute the KKT conditions for the PDE-constrained optimization problem.

4 Inversion Setup and the Simulation Process
4.1 Finite Element Formulation of the Adjoint Problem

The adjoint problem described in Section 3.2.2 can be solved using the Galerkin finite element method. Specifically, Eq. (25) is multiplied by a test function $v(\mathbf{x})$ and integrated over the entire domain Ω. Upon integrating the resulting equation by parts and using a procedure similar to that represented by Eqs. (5) to (9), the weak form of the adjoint problem can be derived as

$$\int_\Omega \sigma \nabla w \cdot \nabla v d\Omega + \sum_{l=1}^{L} \frac{1}{z_l} \int_{\Gamma_{E_l}} (w - W_l)(v - V_l) d\Gamma = \sum_{l=1}^{L} \left(U_l - U_l^{\mathrm{m}} \right) V_l |e_l|, \tag{30}$$

where V_l is a test value used to derive the weak form of Eq. (26a). The adjoint solutions w and W_l can be approximated using Legendre basis functions $\phi_i(\mathbf{x})$ and basis vectors $\mathbf{n}_j$, respectively, as follows:

$$w(\mathbf{x}) \cong w^h(\mathbf{x}) = \sum_{j=1}^{N} \alpha_j^{\mathrm{adj}} \phi_j(\mathbf{x}), \tag{31}$$

$$\mathbf{W} \cong \mathbf{W}^h = \sum_{j=1}^{L-1} \beta_j^{\mathrm{adj}} \mathbf{n}_j, \tag{32}$$

where α_j^{adj} is the nodal value of $w(\mathbf{x})$, β_j^{adj} is the unknown parameter for linearly combining vectors $\mathbf{n}_j$, and $\mathbf{W}^h$ is a vector consisting of W_l at each electrode. The test functions v and V_l are approximated using Eqs. (13) and (14).

Substituting Eqs. (13), (14), (31) and (32) into (30) results in the following linear system of equations:

$$\mathbf{K}^{\mathrm{adj}} \mathbf{u}^{\mathrm{adj}} = \mathbf{F}^{\mathrm{adj}}; \begin{bmatrix} \mathbf{B}^{\mathrm{adj}} & \mathbf{C}^{\mathrm{adj}} \\ \left(-\mathbf{C}^{\mathrm{adj}}\right)^{\mathrm{T}} & \mathbf{D}^{\mathrm{adj}} \end{bmatrix} \begin{bmatrix} \alpha^{\mathrm{adj}} \\ \beta^{\mathrm{adj}} \end{bmatrix} = \begin{bmatrix} 0 \\ \mathbf{I}^{\mathrm{adj}} \end{bmatrix}, \tag{33}$$

where $\mathbf{K}^{\mathrm{adj}}$, $\mathbf{u}^{\mathrm{adj}}$, and $\mathbf{F}^{\mathrm{adj}}$ are the stiffness matrix, solution vector, and right-hand side vector of the adjoint problem, respectively. The superscript "adj" denotes the adjoint problem. The matrices and vectors in Eq. (33) can be written as

$$B_{ij}^{\mathrm{adj}} = \int_{\Omega} \sigma \nabla \phi_i \cdot \nabla \phi_j d\Omega + \sum_{l=1}^{L} \frac{1}{z_l} \int_{\Gamma_{E_l}} \phi_i \phi_j d\Gamma, \quad (1 \le i \le N) \ (1 \le j \le N) \tag{34a}$$

$$C_{ij}^{\mathrm{adj}} = \frac{1}{z_1} \int_{\Gamma_{E_1}} \phi_i d\Gamma - \frac{1}{z_{j+1}} \int_{\Gamma_{E_{j+1}}} \phi_i d\Gamma, \quad (1 \le i \le N) \ (1 \le j \le L-1) \tag{34b}$$

$$\left(-C_{ij}^{\mathrm{adj}}\right)^{\mathrm{T}} = -C_{ji}^{\mathrm{adj}} = -\left(\frac{1}{z_1} \int_{\Gamma_{E_1}} \phi_j d\Gamma - \frac{1}{z_{i+1}} \int_{\Gamma_{E_{i+1}}} \phi_j d\Gamma \right), \quad (1 \le i \le L-1) \ (1 \le j \le N) \tag{34c}$$

$$D_{ij}^{\mathrm{adj}} = \begin{cases} -\dfrac{|e_1|}{z_1}, & i \ne j \\ -\dfrac{|e_1|}{z_1} - \dfrac{|e_{j+1}|}{z_{j+1}}, & i = j \end{cases} \quad (1 \le i \le L-1) \ (1 \le j \le L-1), \tag{34d}$$

$$\mathbf{0} \in R^{N \times 1}, \quad \mathbf{I}^{\mathrm{adj}} = \begin{bmatrix} (U_1 - U_1^{\mathrm{m}})\,|e_1| - (U_2 - U_2^{\mathrm{m}})\,|e_2| \\ (U_1 - U_1^{\mathrm{m}})\,|e_1| - (U_3 - U_3^{\mathrm{m}})\,|e_3| \\ (U_1 - U_1^{\mathrm{m}})\,|e_1| - (U_4 - U_4^{\mathrm{m}})\,|e_4| \\ \vdots \\ (U_1 - U_1^{\mathrm{m}})\,|e_1| - (U_L - U_L^{\mathrm{m}})\,|e_L| \end{bmatrix} \in R^{(L-1) \times 1}, \tag{35}$$

$$\alpha^{\mathrm{adj}} = \begin{bmatrix} \alpha_1^{\mathrm{adj}} \\ \alpha_2^{\mathrm{adj}} \\ \alpha_3^{\mathrm{adj}} \\ \vdots \\ \alpha_N^{\mathrm{adj}} \end{bmatrix} \in R^{N \times 1}, \quad \beta^{\mathrm{adj}} = \begin{bmatrix} \beta_1^{\mathrm{adj}} \\ \beta_2^{\mathrm{adj}} \\ \beta_3^{\mathrm{adj}} \\ \vdots \\ \beta_{L-1}^{\mathrm{adj}} \end{bmatrix} \in R^{(L-1) \times 1}. \tag{36}$$

Solving Eq. (33) yields nodal values of adjoint variable w in the domain as well as the values of β^{adj}. The adjoint variable W_l^h at the electrodes can be derived as

$$\mathbf{W}_l^h = \begin{bmatrix} W_1^h \\ W_2^h \\ W_3^h \\ \vdots \\ W_L^h \end{bmatrix} = \begin{bmatrix} \sum_{l=1}^{L-1} \beta_l^{\mathrm{adj}} \\ -\beta_1^{\mathrm{adj}} \\ -\beta_2^{\mathrm{adj}} \\ \vdots \\ -\beta_{L-1}^{\mathrm{adj}} \end{bmatrix}. \tag{37}$$

The submatrices in Eq. (33) are related to those of the state problem through

$$\mathbf{B}^{\mathrm{adj}} = \mathbf{B}, \tag{38a}$$

$$\mathbf{C}^{\mathrm{adj}} = -\mathbf{C}, \tag{38b}$$

$$\left(-\mathbf{C}^{\mathrm{adj}} \right)^{\mathrm{T}} = \mathbf{C}^{\mathrm{T}}, \tag{38c}$$

$$\mathbf{D}^{\mathrm{adj}} = -\mathbf{D}. \tag{38d}$$

Eq. (38) contributes to reducing the computational cost of constructing the system matrices of the adjoint problem in the inversion process.

4.2 Material Property Update

By solving the state and adjoint problems, the first and second optimality conditions are satisfied. Only the true profile of $\sigma(\mathbf{x})$ exactly satisfies the control problem represented by Eqs. (28) and (29). Therefore, the material profile $\sigma(\mathbf{x})$ must be updated to satisfy the third optimality condition. Updating $\sigma(\mathbf{x})$ to minimize the Lagrangian $\mathcal{L}$ requires a reduced gradient for $\mathcal{L}$. The process of updating the control variable $\sigma(\mathbf{x})$ using the state and adjoint solutions can be summarized as follows:

1) Assuming the initial profile of $\sigma(\mathbf{x})$, solve the forward problem (1) and (2) for state variables $u(\mathbf{x})$ and U_l.

2) Using the state solution U_l, solve the adjoint problem (25) and (26) for adjoint solutions $w(\mathbf{x})$ and W_l.

3) Using the state and adjoint solutions, calculate the reduced gradient for $\mathcal{L}$ with respect to the control variable $\sigma(\mathbf{x})$ as

$$g_\sigma \equiv \nabla_\sigma \mathcal{L} = -R_\sigma \Delta \sigma - \nabla w \cdot \nabla u = -R_\sigma \left(\frac{\partial^2 \sigma}{\partial x^2} + \frac{\partial^2 \sigma}{\partial y^2} \right) + \left(-\frac{\partial w}{\partial x} \frac{\partial u}{\partial x} - \frac{\partial w}{\partial y} \frac{\partial u}{\partial y} \right), \tag{39}$$

where the derivatives are calculated using second-order accurate finite difference methods. When using a radial mesh, such as that shown in Fig. 5a, the reduced gradient (40) expressed in a cylindrical coordinate system can be used

$$g_\sigma = -R_\sigma \left(\frac{\partial^2 \sigma}{\partial r^2} + \frac{1}{r} \frac{\partial \sigma}{\partial r} + \frac{1}{r^2} \frac{\partial^2 \sigma}{\partial \theta^2} \right) + \left(-\frac{\partial w}{\partial r} \frac{\partial u}{\partial r} - \frac{1}{r^2} \frac{\partial w}{\partial \theta} \frac{\partial u}{\partial \theta} \right). \tag{40}$$

4) Determine the search direction using a line search method and update the electrical conductivity profile $\sigma(\mathbf{x})$.

4.2.1 Conjugate Gradient Method with Inexact Line Search

In this study, the search direction for the optimal solution of the control variable σ is determined using the Flétcher-Reeves conjugate gradient method with an inexact line search. The continuous form of the reduced gradient, Eqs. (39) or (40), can be discretized by being evaluated at each nodal point. Let $\mathbf{g}_k$ denote the discrete reduced gradient at the kth inversion iteration,

$$\mathbf{g}_k = (\nabla_\sigma \mathcal{L})_k . \tag{41}$$

Then, the electrical conductivity vector $\boldsymbol{\sigma}_k$ comprising nodal values of σ is updated via

$$\boldsymbol{\sigma}_{k+1} = \boldsymbol{\sigma}_k + \alpha \mathbf{d}_k, \tag{42}$$

where $\mathbf{d}_k$ is a search direction vector at σ_k, and α is the step length in the direction of $\mathbf{d}_k$. By using the Flétcher-Reeves method, the search direction vector is calculated as

$$\mathbf{d}_k = \begin{cases} -\mathbf{g}_k, & k = 0, \\ -\mathbf{g}_k + \dfrac{\mathbf{g}_k \cdot \mathbf{g}_k}{\mathbf{g}_{k-1} \cdot \mathbf{g}_{k-1}} \mathbf{d}_{k-1}, & k \geq 1. \end{cases} \tag{43}$$

The misfit functional is evaluated using the updated electrical conductivity $\boldsymbol{\sigma}_{k+1}$ and is compared to a preset tolerance. If it does not meet the tolerance criterion, the inversion process set $k \leftarrow k+1$ and proceeded to the next iteration. As is known, the discrete search direction vector $\mathbf{d}_k$ gradually deviates from the direction to a local minimum because of the non-optimal step length α and the round-off error arising from the accumulation of the $\mathbf{g}_k \cdot \mathbf{g}_k / \mathbf{g}_{k-1} \cdot \mathbf{g}_{k-1}$ terms in Eq. (43). Therefore, it is necessary to reset $\mathbf{d}_{m+1}$ to $-\mathbf{g}_{m+1}$ after every mth iteration.

In this study, an inexact line search method is used to determine a step length α that would yield an adequate reduction in the objective functional J. Specifically, the method requires the step length to reduce the objective functional sufficiently, as indicated by the *Armijo condition* (or *sufficient decrease condition*); this condition is expressed as

$$J(\boldsymbol{\sigma}_k + \alpha \mathbf{d}_k) \leq J(\boldsymbol{\sigma}_k) + \overline{\mu} \alpha \mathbf{g}_k \cdot \mathbf{d}_k, \tag{44}$$

where $\overline{\mu}$ is selected to be a small value, which is $\overline{\mu} = 10^{-10}$ in this study. To satisfy the Armijo condition, the backtracking algorithm described in Table 2 can be used. In this procedure, an initial step length $\overline{\alpha}$ is set at the beginning. If Eq. (44) is violated during the inversion, the step length is iteratively reduced by setting $\alpha \leftarrow \overline{\rho} \alpha$. In this study, $\overline{\rho} = 0.5$ is used.

Table 2: Backtracking algorithm to determine the step length $\boldsymbol{\alpha}$

Choose $\overline{\alpha} > 0$, $\overline{\alpha}, \overline{\mu} \in (0, 1)$; set $\alpha \leftarrow \overline{\alpha}$;
repeat $\alpha \leftarrow \overline{\rho} \alpha$;
until $J(\boldsymbol{\sigma}_k + \alpha \mathbf{d}_k) \leq J(\boldsymbol{\sigma}_k) + \overline{\mu} \alpha \mathbf{g}_k \cdot \mathbf{d}_k$
Terminate with $\alpha_k = \alpha$

4.2.2 Regularization Factor Continuation Scheme

The choice of the regularization factor R_σ in Eqs. (39) or (40) considerably affects the reconstruction of the electrical conductivity profile. If R_σ is excessively large, it may be difficult to capture a sharply varying interface in the profile because of the large penalty on the gradient of $\sigma(\mathbf{x})$. Conversely,

if R_σ is excessively small, the inversion may suffer from a solution multiplicity problem. To determine the optimal regularization factor at each inversion iteration, a regularization factor continuation scheme [24–26] is used in this study. The reduced gradient in Eqs. (39) or (40) can be formally rewritten as

$$\nabla_\sigma \mathcal{L} = R_\sigma \left(\nabla_\sigma J_{\mathrm{r}} \right) + \nabla_\sigma J_{\mathrm{m}}, \tag{45}$$

in which

$$\nabla_\sigma J_{\mathrm{r}} = -\Delta\sigma, \tag{46a}$$

$$\nabla_\sigma J_{\mathrm{m}} = -\nabla w \cdot \nabla u. \tag{46b}$$

In Eq. (45), $R_\sigma (\nabla_\sigma J_{\mathrm{r}})$ represents the gradient of the regularization functional, and $\nabla_\sigma J_{\mathrm{m}}$ denotes the gradient of the misfit functional. The first term, $R_\sigma (\nabla_\sigma J_{\mathrm{r}})$, penalizes spatial oscillations in the inverted profile such that an increasing R_σ results in a smoother inverted profile. A balance between these two terms can be imposed using

$$R_\sigma \left| \nabla_\sigma J_{\mathrm{r}} \right| < \left| \nabla_\sigma J_{\mathrm{m}} \right| \implies R_\sigma < \frac{\left| \nabla_\sigma J_{\mathrm{m}} \right|}{\left| \nabla_\sigma J_{\mathrm{r}} \right|}. \tag{47}$$

Therefore, R_σ can be calculated at each iteration as

$$R_\sigma = \varepsilon \frac{\left| \nabla_\sigma J_{\mathrm{m}} \right|}{\left| \nabla_\sigma J_{\mathrm{r}} \right|}, (0 \le \varepsilon \le 1), \tag{48}$$

where the value of the weight factor ε is between 0.5 and 1, as recommended for a reasonable regularization effect.

5 Numerical Results

5.1 Homogeneous Domains

Consider a circular domain with a radius of 15 cm, as shown in Fig. 8. A total of 32 electrodes is placed on the boundary and spaced evenly to cover 50% of the boundary. For finite element implementation, the mixed mesh illustrated in Fig. 5b is used. The contact impedance of the electrodes is $0.22 \ \Omega \cdot \mathrm{cm}^2$. The initial value of the regularization factor R_σ is 1.0, and the weight factor ε for the regularization factor continuation scheme is 0.5. As an excitation to the domain, a current with a cosine pattern, as expressed in Eq. (49), is input to each electrode along the circular perimeter,

$$I_l = \cos(2\pi l/32), l = 1, 2, \ldots, 32. \tag{49}$$

Fig. 9 shows the target, initial guess, and reconstructed electrical conductivity profiles. The target profile is homogeneous with $\sigma_{\mathrm{tg}} = 1.0$ S/cm, which is typical of graphite materials. The inversion starts with an initial guess of $\sigma_{\mathrm{ini}} = 0.5$ S/cm and reconstructs the target profile accurately at about 700 iterations. Fig. 9d shows the response misfit as a function of the iteration number during the inversion process. The misfit decreases from 3×10^2 to 1.49×10^{-3}, which represents a reduction on the order of 10^{-5}. The response misfit, $\mathcal{F}_m$, as part of the objective functional J in Eq. (21), can be written as

$$\mathcal{F}_m = \frac{1}{2} \sum_{l=1}^{L} \int_{\Gamma_{E_l}} \left(U_l - U_l^{\mathrm{m}} \right)^2 d\Gamma. \tag{50}$$
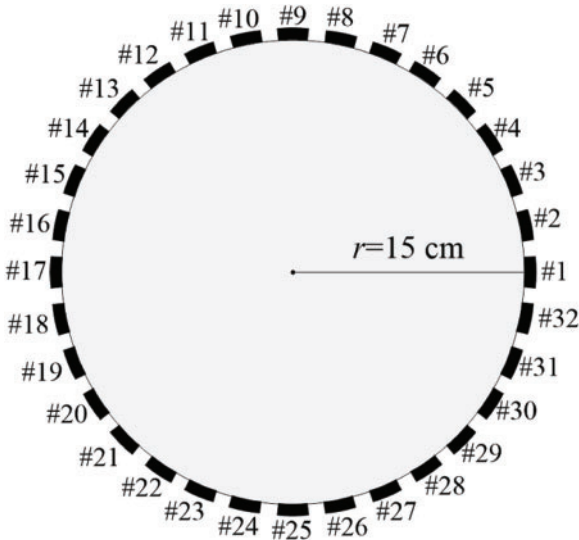
Figure 8: Schematic of a circular domain and 32 surface electrodes used for inversion
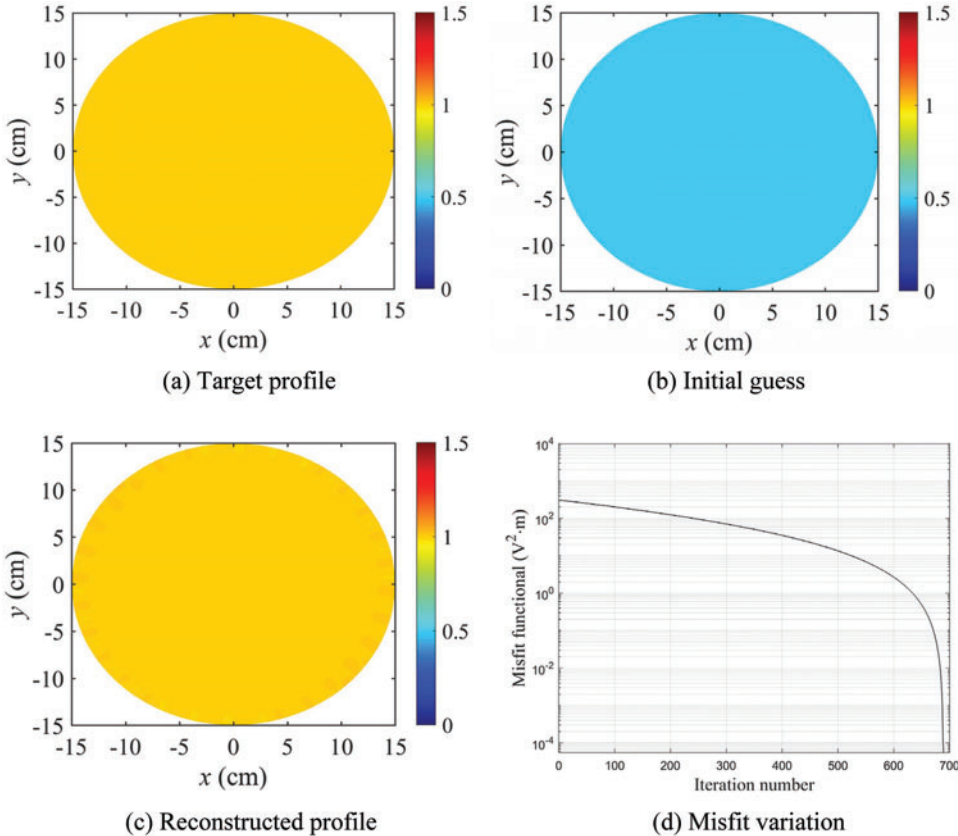
Figure 9: Numerical inversion for homogeneous target profile

To investigate the accuracy of the inversion result, the errors in the inverted electrical conductivity values are calculated at four sampling points, as shown in Fig. 10: A(0,0), B(4,0), C(8,0), and D(12,0). Table 3 lists the errors at each sampling point. The maximum error is 0.116%, which demonstrates that the inversion for the homogeneous electrical conductivity profile is highly accurate.
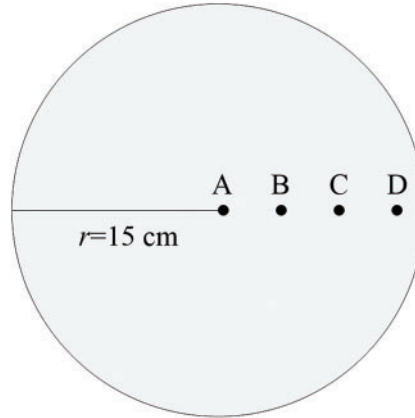
Figure 10: Sampling points for error calculation

Table 3: Errors in the inverted electrical conductivity values at the sampling points (inversion case with $\sigma_{tg} = 1.0$ S/cm and $\sigma_{ini} = 0.5$ S/cm)

Point	Target σ (S/cm)	Reconstructed σ (S/cm)	Error (%)
A	1.00000	1.00002	0.002
B	1.00000	0.99999	0.001
C	1.00000	1.00026	0.026
D	1.00000	1.00116	0.116

To investigate the effect of the initial guess on the reconstructed profile, four cases of the inversion with different initial-to-target ratios are considered. Table 4 shows the four cases for the initial guess σ_{ini} and target σ_{tg}. For Cases 1 and 2, the initial guess is less than the target, whereas for Cases 3 and 4, it is greater. The electrode arrangement, input current, and contact impedance are the same as those in the previous example.

Table 4: Four cases of inversion with different initial-to-target ratios

Case	Target electrical conductivity σ_{tg} (S/cm)	Assumed electrical conductivity σ_{ini} (S/cm)	σ_{ini}/σ_{tg}
1	1.5	0.7	0.47
2	15.0	1.5	0.10
3	1.5	2.3	1.53
4	1.0	10.0	10.00

Figs. 11–14 display the inversion results for the four electrical conductivity profiles presented in Table 4. In all four cases, the homogeneous target values are accurately reconstructed. In particular, as shown in Figs. 12b and 14b, the target values are recovered well even when the target is 10 times smaller or larger than the initial guess. Figs. 11c, 12c, 13c and 14c show the misfit $\mathcal{F}_m$ as a function of the number of iterations. For each case, the misfit decreases by a factor of at least 10^{-5}. Figs. 11d, 12d, 13d and 14d show the electric potential values at the 32 electrodes calculated using the reconstructed electrical conductivity profile for each case. The calculated electric potential values nearly coincide with the measured values, which demonstrates that the target profiles are successfully reconstructed. The root-mean-square (RMS) error, e_{RMS}, and the relative RMS error, $e_{\text{r,RMS}}$, of the electric potential at the electrodes can be calculated using Eq. (51). In the equations, U_i and U_i^m denote the calculated and measured electric potential values at the ith electrode, respectively, and $|U^m|_{\text{max}}^2$ is the absolute maximum of the measured potentials. Table 5 shows the calculated RMS errors for each case of the inversion process. Even in Case 4 with the largest relative error, the value is less than 0.18%. In all cases, the inversion results are evaluated to be sufficiently accurate,

$$e_{\text{RMS}} = \sqrt{\frac{1}{L} \sum_{i=1}^{L} \left(U_i - U_i^m\right)^2}, \quad e_{\text{r,RMS}} = \sqrt{\frac{1}{L} \sum_{i=1}^{L} \frac{\left(U_i - U_i^m\right)^2}{|U^m|_{\text{max}}^2}}. \tag{51}$$

(a) Initial guess

(b) Reconstructed profile at 760 iterations

(c) Misfit variation

(d) Recovered potentials at electrodes
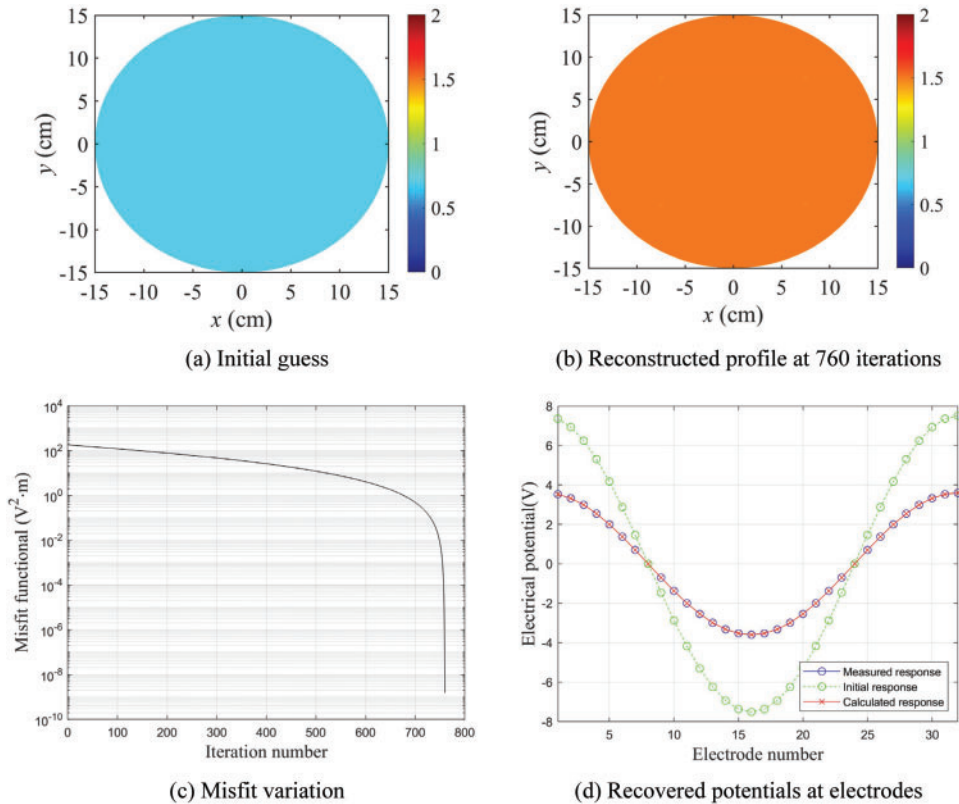
Figure 11: Inversion results for Case 1; $\sigma_{\text{tg}} = 1.5$ S/cm, $\sigma_{\text{ini}} = 0.7$ S/cm

(a) Initial guess

(b) Reconstructed profile at 2290 iterations

(c) Misfit variation

(d) Recovered potentials at electrodes
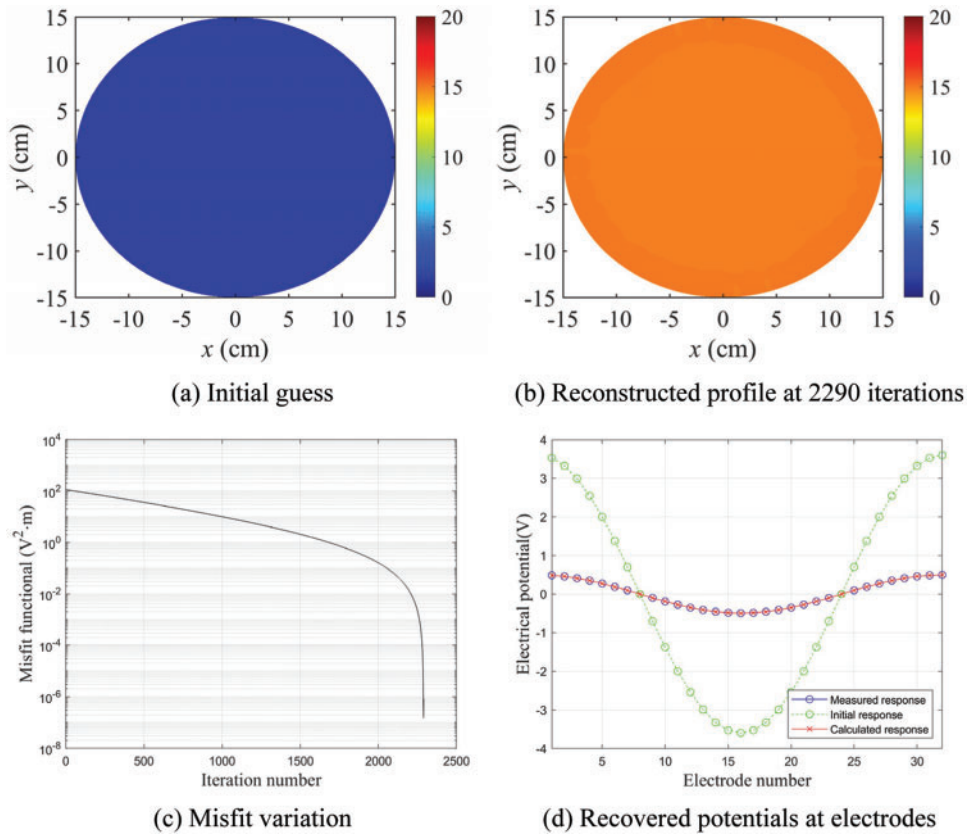
Figure 12: Inversion results for Case 2; $\sigma_{tg} = 15.0$ S/cm, $\sigma_{ini} = 1.5$ S/cm

(a) Initial guess

(b) Reconstructed profile at 430 iterations

Figure 13: (Continued)

(c) Misfit variation

(d) Recovered potentials at electrodes
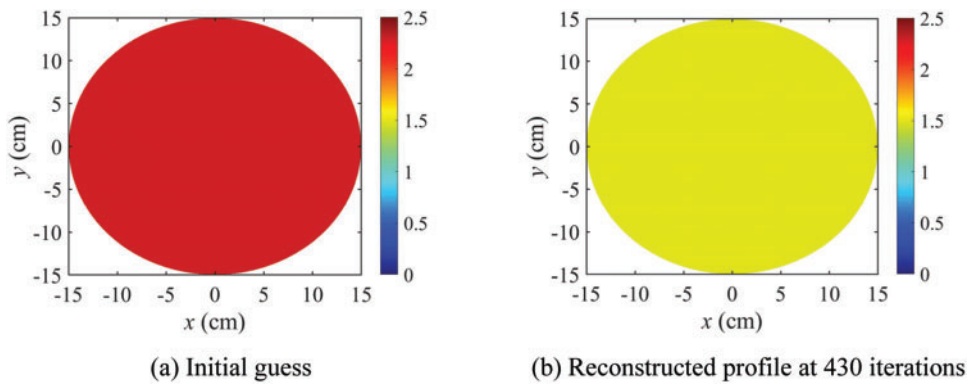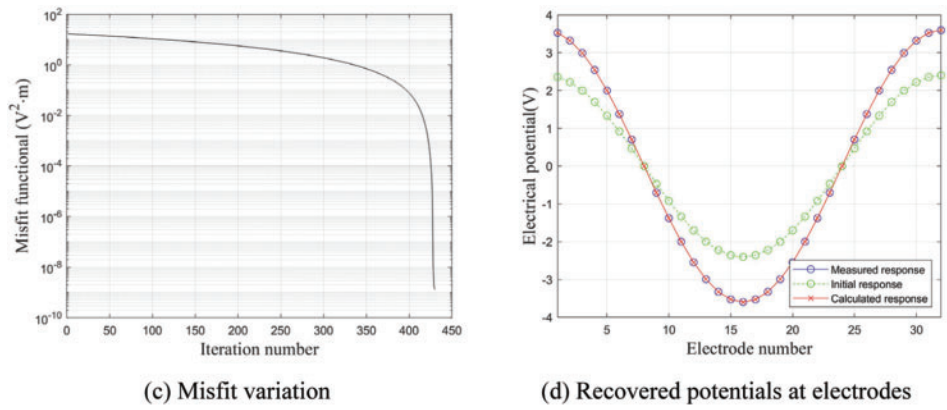
Figure 13: Inversion results for Case 3; $\sigma_{tg} = 1.5$ S/cm, $\sigma_{ini} = 2.3$ S/cm

(a) Initial guess

(b) Reconstructed profile at 400 iterations

(c) Misfit variation

(d) Recovered potentials at electrodes
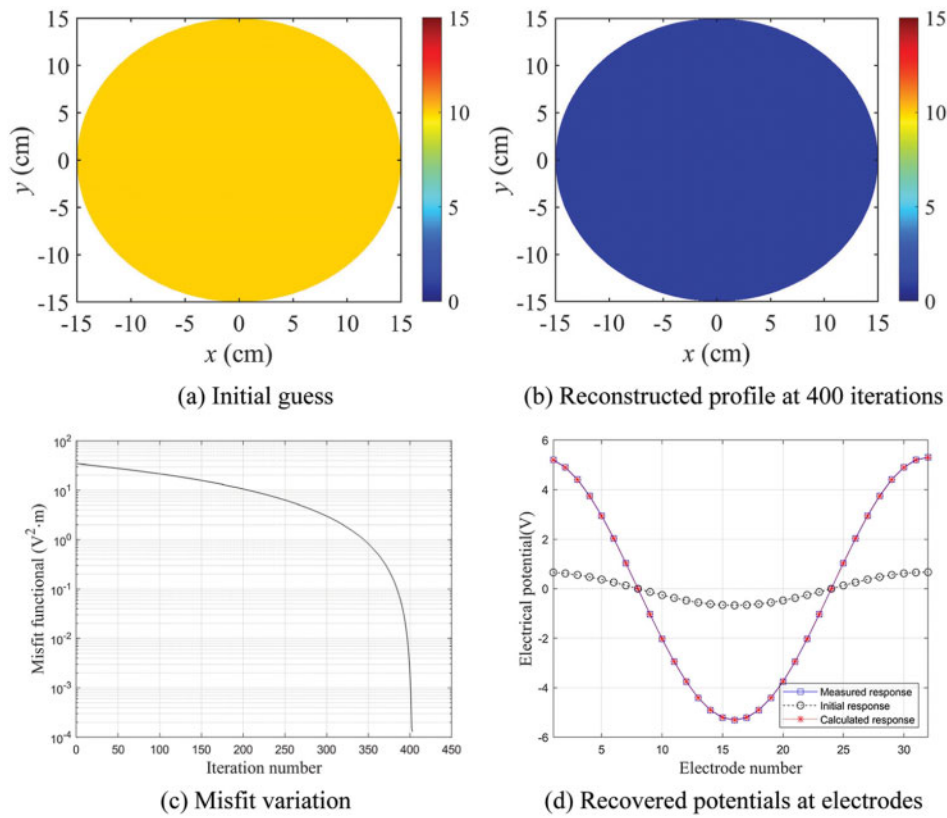
Figure 14: Inversion results for Case 4; $\sigma_{tg} = 1.0$ S/cm, $\sigma_{ini} = 10.0$ S/cm

Table 5: RMS errors of the reconstructed homogeneous profiles

RMS errors	Case 1	Case 2	Case 3	Case 4
e_{RMS} (V)	8.11×10^{-6}	1.86×10^{-4}	7.55×10^{-6}	9.25×10^{-3}
$e_{r,RMS}$	2.25×10^{-6}	3.74×10^{-4}	2.10×10^{-6}	1.74×10^{-3}

5.2 Heterogeneous Domains

Next, the inversion is performed to reconstruct heterogeneous electrical conductivity profiles. Fig. 15 shows three cases of the target profile. In Case 5, the target values of the electrical conductivity are 0.04 S/cm for $y \geq 0$ and 0.01 S/cm for $y < 0$. In Case 6, the target profile is divided into three layers: 0.04 S/cm for $y \geq 5$, 0.025 S/cm for $-5 \leq y < 5$, and 0.01 S/cm for $y < -5$. The target profile for Case 7 has four quadrants. In quadrants 1 and 3, the target value is 0.04 S/cm. In quadrants 2 and 4, the target value is 0.01 S/cm. The target conductivity values of Case 5 to Case 7 are typical of air-dried concrete materials in various conditions [27]. Examples of the profile heterogeneity in Fig. 15 include fiber-reinforced composite sandwich plates and concrete specimens under curing. The electrode arrangement, current input, contact impedance, initial value of R_σ, and weight factor ε are the same as in the homogeneous domain cases.

(a) Case 5: two layers

(b) Case 6: three layers

(c) Case 7: arbitrary heterogeneous profile
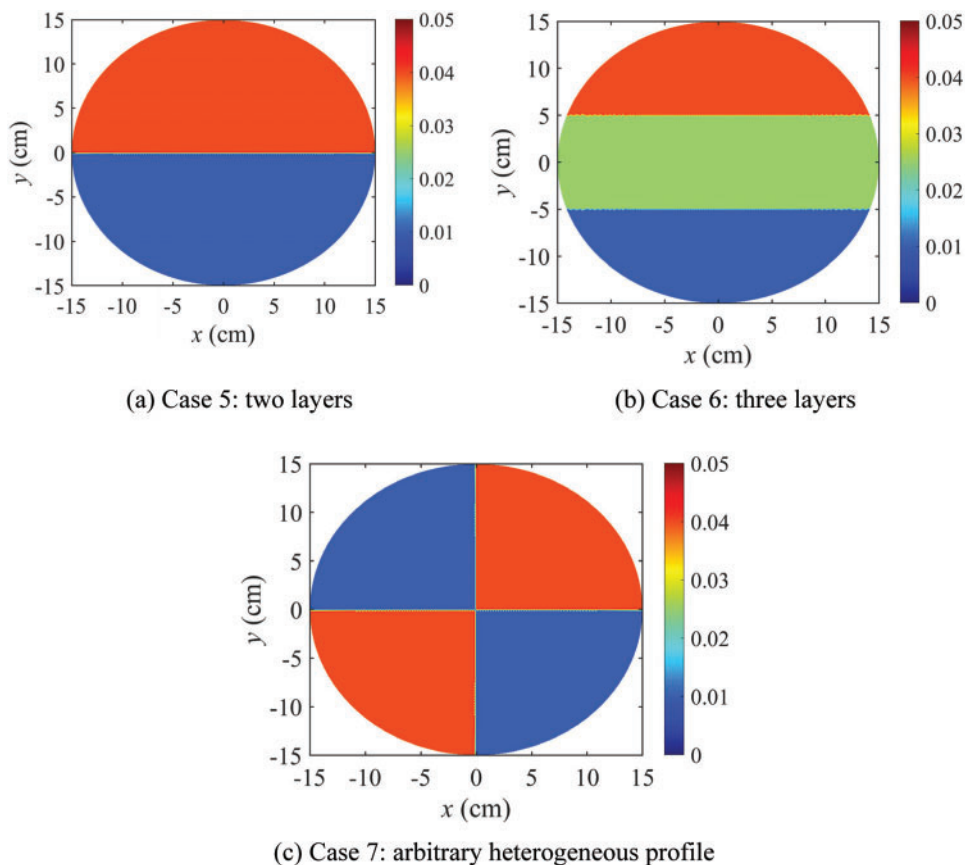
Figure 15: Heterogeneous target electrical conductivity profiles

Figs. 16–18 show the inversion results for the heterogeneous electrical conductivity profiles. The target conductivity values are reconstructed reasonably well in the three heterogeneous cases. Figs. 16c, 17c, and 18c show the response misfit $\mathcal{F}_m$ as a function of the iteration number. Figs. 16d, 17d, and 18d show the electric potential values calculated at the electrodes using the reconstructed electrical conductivity profile for each case. The calculated electric potential values nearly coincide with the measured ones, which demonstrates that the reconstructed profiles converged to the targets. For each case, the initial misfit decreases by a factor on the order of 10^{-3}. Table 6 shows the RMS error and the relative RMS error of the electrical potentials calculated at the electrodes for each case. The errors were

calculated using Eq. (51). They are relatively large compared with those in the homogeneous cases, due to the difficulty in accurately recovering the sharply varying interfaces between layers. Nevertheless, the relative RMS error of the heterogeneous cases is less than 0.80%, indicating that the inversion results are sufficiently accurate.

(a) Initial guess; $\sigma_{\text{ini}} = 0.025$ S/cm

(b) Reconstructed profile at 600 iterations

(c) Misfit variation

(d) Recovered potentials at electrodes
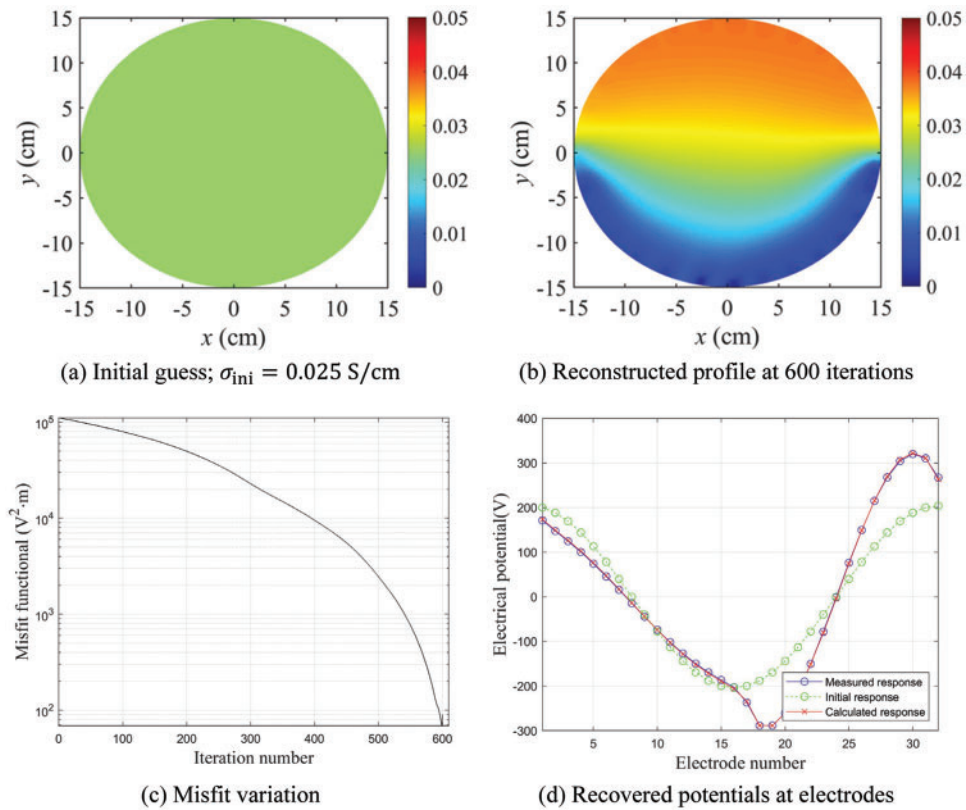
Figure 16: Inversion results for Case 5

(a) Initial guess; $\sigma_{\text{ini}} = 0.025$ S/cm

(b) Reconstructed profile at 495 iterations

Figure 17: (Continued)

(c) Misfit variation   (d) Recovered potentials at electrodes
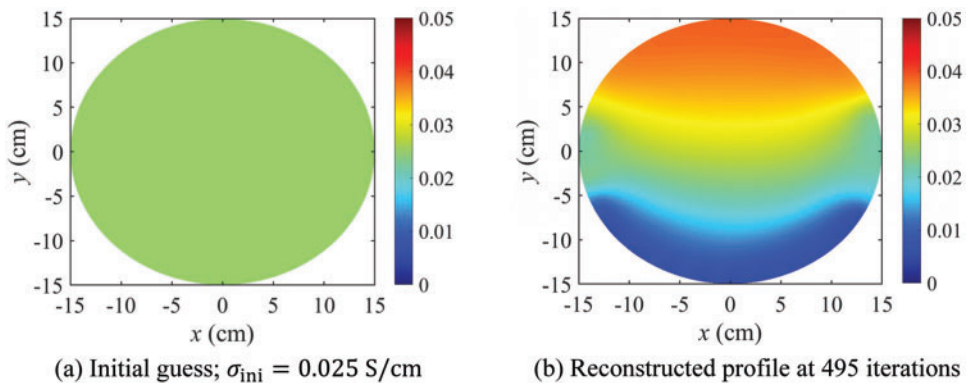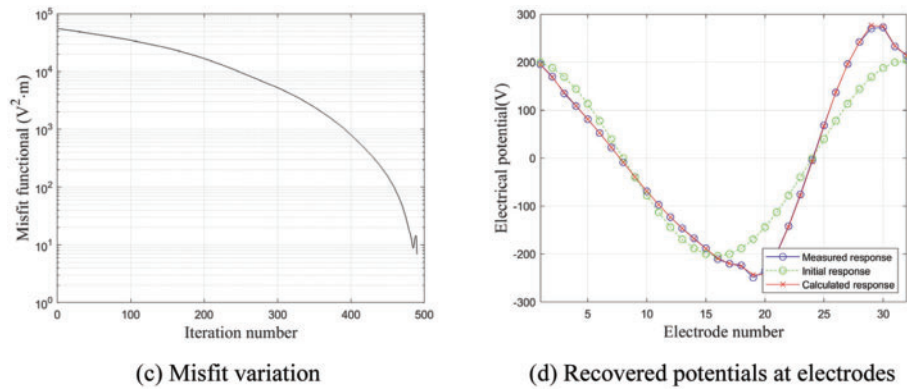
Figure 17: Inversion results for Case 6

(a) Initial guess; $\sigma_{\text{ini}} = 0.025$ S/cm   (b) Reconstructed profile at 760 iterations

(c) Misfit variation   (d) Recovered potentials at electrodes
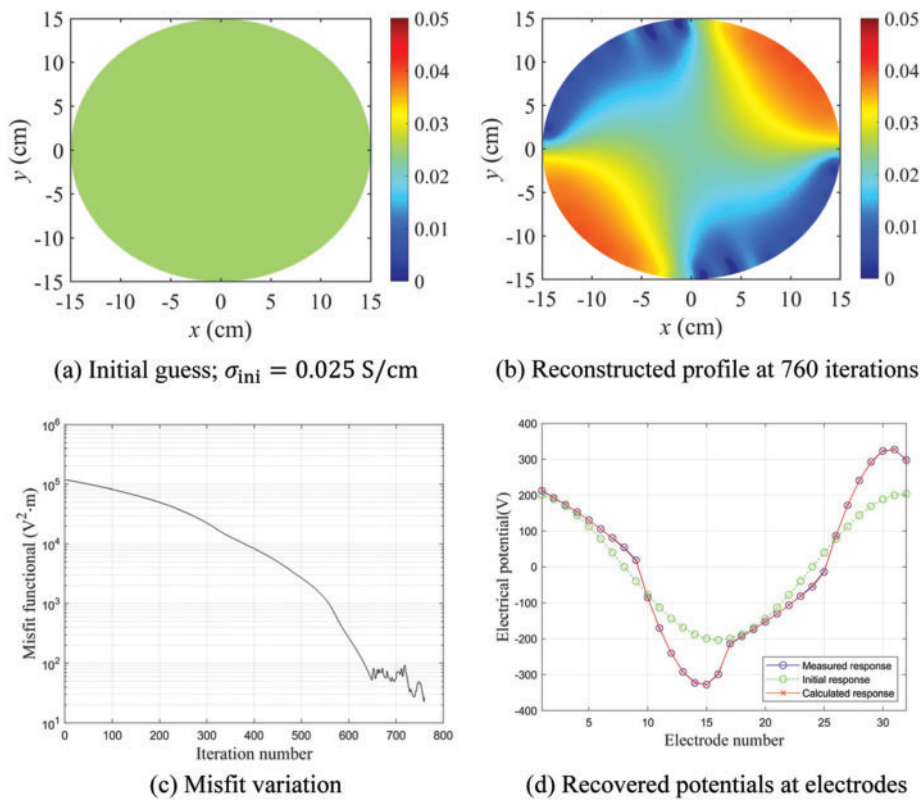
Figure 18: Inversion results for Case 7

Table 6: RMS errors of the reconstructed heterogeneous profiles

RMS errors	Case 5	Case 6	Case 7
e_{RMS} (V)	1.96×10^{0}	2.18×10^{0}	1.08×10^{0}
$e_{\text{r,RMS}}$	6.13×10^{-3}	8.00×10^{-3}	3.28×10^{-3}

6 Conclusions

This study was conducted to develop a nonlinear inversion method for electrical impedance tomography of structures using measured electric potentials at the surface. The proposed method minimizes the misfit between calculated and measured electric potential values at surface electrodes within a PDE-constrained optimization framework. The CEM was used as a forward model to calculate the electric potential due to current input. By solving the KKT conditions of the Lagrangian iteratively, the inversion procedure could successfully recover heterogeneous electrical conductivity profiles. The TN regularization scheme was used to mitigate the ill-posedness of the inverse problem and improve the convergence of the solution. A series of numerical results showed that the homogeneous and heterogeneous electrical conductivity profiles were successfully reconstructed using the inversion method developed in this study.

For all numerical example cases, the misfit was decreased from its original value by a factor on the order of 10^{-4} or less. In addition, the electric potential values at the electrodes that were calculated using the reconstructed conductivity profiles were nearly identical to the measured values. Specifically, the relative RMS error of the calculated electric potential after inversion was less than 0.18% for the homogeneous cases. The relative RMS error of the heterogeneous cases was less than 0.80%, indicating that the inversion results are sufficiently accurate. This study is expected to provide an application framework for nondestructive evaluation of structures, geotechnical site characterization, etc.

Conflicts of Interest: The authors declare that they have no conflicts of interest to report regarding the present study.

References

1. Paipetis, A. S., Matikas, T. E., Aggelis, D. G., van Hemelrijck, D. (2012). *Emerging technologies in non-destructive testing*. London: CRC Press.

2. Kralovec, C., Schagerl, M. (2020). Review of structural health monitoring methods regarding a multi-sensor approach for damage assessment of metal and composite structures. *Sensors, 20(3),* 826. DOI 10.3390/s20030826.

3. Nachman, A. I. (1988). Reconstruction from boundary measurements. *Annals of Mathematics, 128(3),* 531–576. DOI 10.2307/1971435.

4. Vauhkonen, M. (1997). *Electrical impedance tomography and prior information*. Finland: Kuopio University.

5. Borsic, A., Lionheart, W. R. B., McLeod, C. N. (2002). Generation of anisotropic-smoothness regularization Filters for EIT. *IEEE Transactions on Medical Imaging, 21(6),* 579–587. DOI 10.1109/TMI.2002.800611.

6. Kaipio, J. P., Kolehmainen, V., Somersalo, E., Vauhkonen, M. (2000). Statistical inversion and Monte Carlo sampling methods in electrical impedance tomography. *Inverse Problems, 16(5),* 1487–1522. DOI 10.1088/0266-5611/16/5/321.

7. Santosa, M., Vogelius, M. (1990). A back projection algorithm for electrical impedance imaging. *SIAM Journal on Applied Mathematics, 50(1),* 216–243. DOI 10.1137/0150014.

8. Cheney, M., Isaacson, D., Newell, J. C., Simske, S., Goble, J. (1990). Noser: An algorithm for solving the inverse conductivity problem. *International Journal of Imaging Systems and Technology, 2(2),* 66–75. DOI 10.1002/(ISSN)1098-1098.

9.   Knudsen, K., Lassas, M., Mueller, J. L., Siltanen, S. (2009). Regularized D-bar method for the inverse conductivity problem. *Inverse Problems and Imaging, 3(4),* 599–624. DOI 10.3934/ipi.2009.3.599.

10. Abbasi, A., Vahdat, B. V. (2010). A non-iterative linear inverse solution for the block approach in EIT. *Journal of Computational Science, 1(4),* 190–196. DOI 10.1016/j.jocs.2010.09.001.

11. Hamilton, S. J., Hauptmann, A. (2018). Deep D-bar: Real-time electrical impedance tomography imaging with deep neural networks. *IEEE Transactions on Medical Imaging, 37(10),* 2367–2377. DOI 10.1109/TMI.2018.2828303.

12. Jordana, J., Gasulla, M., Pallas-Areny, R. (2001). Electrical resistance tomography to detect leaks from buried pipes. *Measurement Science and Technology, 12(8),* 1061–1068. DOI 10.1088/0957-0233/12/8/311.

13. Baltopoulos, A., Polydorides, N., Pambaguian, L., Vavouliotis, A., Kostopoulos, V. (2012). Damage identification in carbon fiber reinforced polymer plates using electrical resistance tomography mapping. *Journal of Composite Materials, 47(26),* 3285–3301. DOI 10.1177/0021998312464079.

14. Vauhkonen, P. J., Vauhkonen, M., Savolainen, T., Kaipio, J. P. (1999). Three-dimensional electrical impedance tomography based on the complete electrode model. *IEEE Transactions on Biomedical Engineering, 46(9),* 1150–1160. DOI 10.1109/10.784147.

15. Agsten, B. (2015). *Comparing the complete and the point electrode model for combining TCS and EEG (Master Thesis).* Westfälische Wilhelms-Universität Münster, Germany.

16. Hadinia, M., Jafari, R., Soleimani, M. (2016). EIT image reconstruction based on a hybrid FE-EFG forward method and the complete-electrode model. *Physiological Measurement, 37(6),* 863–878. DOI 10.1088/0967-3334/37/6/863.

17. Garrillo, M., Gómez, J. A. (2015). A globally convergent algorithm for a PDE-constrained optimization problem arising in electrical impedance tomography. *Numerical Functional Analysis and Optimization, 36(6),* 748–776. DOI 10.1080/01630563.2015.1031379.

18. Albuquerque, Y. F., Laurain, A., Sturm, K. (2020). A shape optimization approach for electrical impedance tomography with point measurements. *Inverse Problems, 36(9),* 095006. DOI 10.1088/1361-6420/ab9f87.

19. Gupta, M., Mishra, R. K., Roy, S. (2020). Sparse reconstruction of log-conductivity in current density impedance tomography. *Journal of Mathematical Imaging and Vision, 62(2),* 189–205. DOI 10.1007/s10851-019-00929-5.

20. Abdulla, U. G., Bukshtynov, V., Seif, S. (2021). Cancer detection through electrical impedance tomography and optimal control theory: Theoretical and computational analysis. *Mathematical Biosciences and Engineering, 18(4),* 4834–4859. DOI 10.3934/mbe.2021246.

21. Pasha, M., Kupis, S., Ahmad, S., Khan, T. (2021). A Krylov subspace type method for electrical impedance tomography. *ESIAM: Mathemetical Modelling and Numerical Analysis, 55(6),* 2827–2847. DOI 10.1051/m2an/2021057.

22. Cheng, K., Isaacson, D., Newell, J. C., Gisser, D. G. (1989). Electrode models for electric current computed tomography. *IEEE Transactions on Biomedical Engineering, 36(9),* 918–924. DOI 10.1109/10.35300.

23. Saha, S. K. (2013). *Technology computer aided design: Simulation for VLSI MOSFET.* London: CRC Press.

24. Kang, J. W., Kallivokas, L. F. (2010). The inverse medium problem in 1D PML-truncated heterogeneous semi-infinite domains. *Inverse Problems in Science and Engineering, 18(6),* 759–786. DOI 10.1080/17415977.2010.492510.

25. Kang, J. W., Kallivokas, L. F. (2011). The inverse medium problem in heterogeneous PML-truncated domains using scalar probing waves. *Computer Methods in Applied Mechanics and Engineering, 200(1–4),* 265–283. DOI 10.1016/j.cma.2010.08.010.

26. Joh, N., Kang, J. W. (2021). Material profile reconstruction using plane electromagnetic waves in PML-truncated heterogeneous domains. *Applied Mathematical Modeling, 96(6),* 813–833. DOI 10.1016/j.apm.2021.03.026.

27. Neville, A. M. (1995). *Properties of concrete.* London: Longman.

Appendix A. Finite Differences for a Non-Unifrom Grid

In a uniform finite-element mesh, as shown in Fig. A1, the first-order and second-order derivatives at node (i, j) can be calculated using the central difference method, as shown in Eqs. (A1)–(A4):

$$\frac{\partial u_{i,j}}{\partial x} = \frac{u_{i+1,j} - u_{i-1,j}}{2\Delta x}, \tag{A1}$$

$$\frac{\partial u_{i,j}}{\partial y} = \frac{u_{i,j+1} - u_{i,j-1}}{2\Delta y}, \tag{A2}$$

$$\frac{\partial^2 u_{i,j}}{\partial x^2} = \frac{u_{i+1,j} - 2u_{i,j} + u_{i-1,j}}{\Delta x^2}, \tag{A3}$$

$$\frac{\partial^2 u_{i,j}}{\partial y^2} = \frac{u_{i,j+1} - 2u_{i,j} + u_{i,j-1}}{\Delta y^2}, \tag{A4}$$

where Δx and Δy are the spacing between node (i, j) and the adjacent nodes in the x and y directions, respectively. For nodes located at the boundary, derivatives cannot be calculated using the central difference method, as adjacent nodes exist in only one direction.
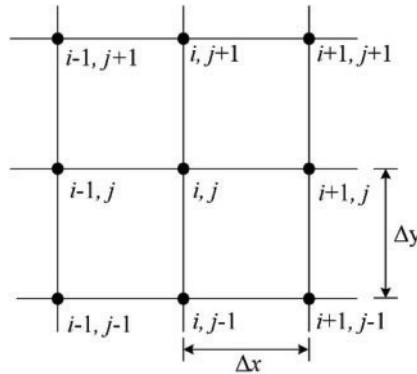
Figure A1: Uniform finite element mesh

This study used the backward difference method shown in Eqs. (A5)–(A8) to calculate the derivative at nodes located at the boundary:

$$\frac{\partial u_{i,j}}{\partial x} = \frac{3u_{i,j} - 4u_{i-1,j} + u_{i-2,j}}{2\Delta x}, \tag{A5}$$

$$\frac{\partial u_{i,j}}{\partial y} = \frac{3u_{i,j} - 4u_{i,j-1} + u_{i,j-2}}{2\Delta y}, \tag{A6}$$

$$\frac{\partial^2 u_{i,j}}{\partial x^2} = \frac{2u_{i,j} - 5u_{i-1,j} + 4u_{i-2,j} - u_{i-3,j}}{\Delta x^2}, \tag{A7}$$

$$\frac{\partial^2 u_{i,j}}{\partial y^2} = \frac{2u_{i,j} - 5u_{i,j-1} + 4u_{i,j-2} - u_{i,j-3}}{\Delta y^2}. \tag{A8}$$

For a radial finite-element mesh such as that shown in Fig. A2, the polar coordinate system can be used to calculate the derivative.
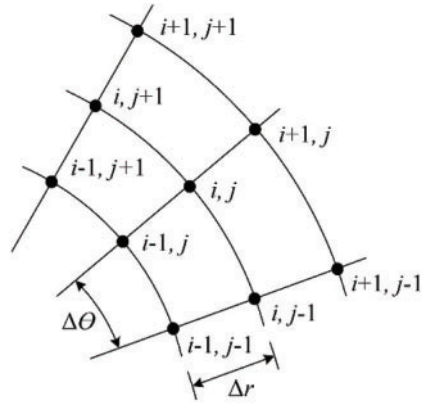
Figure A2: Polar coordinate system finite element mesh

The central difference method for the polar coordinate system is shown in

$$\frac{\partial u_{i,j}}{\partial r} = \frac{u_{i+1,j} - u_{i-1,j}}{2\Delta r}, \tag{A9}$$

$$\frac{\partial u_{i,j}}{\partial \theta} = \frac{u_{i,j+1} - u_{i,j-1}}{2\Delta \theta}, \tag{A10}$$

$$\frac{\partial^2 u_{i,j}}{\partial r^2} = \frac{u_{i+1,j} - 2u_{i,j} + u_{i-1,j}}{\Delta r^2}, \tag{A11}$$

$$\frac{\partial^2 u_{i,j}}{\partial \theta^2} = \frac{u_{i,j+1} - 2u_{i,j} + u_{i,j-1}}{\Delta \theta^2}, \tag{A12}$$

where r and θ are the radial and angular coordinates, respectively. The backward difference method for the polar coordinate system can be expressed as

$$\frac{\partial u_{i,j}}{\partial r} = \frac{3u_{i,j} - 4u_{i-1,j} + u_{i-2,j}}{2\Delta r}, \tag{A13}$$

$$\frac{\partial u_{i,j}}{\partial \theta} = \frac{3u_{i,j} - 4u_{i,j-1} + u_{i,j-2}}{2\Delta \theta}, \tag{A14}$$

$$\frac{\partial^2 u_{i,j}}{\partial r^2} = \frac{2u_{i,j} - 5u_{i-1,j} + 4u_{i-2,j} - u_{i-3,j}}{\Delta r^2}, \tag{A15}$$

$$\frac{\partial^2 u_{i,j}}{\partial \theta^2} = \frac{2u_{i,j} - 5u_{i,j-1} + 4u_{i,j-2} - u_{i,j-3}}{\Delta \theta^2}. \tag{A16}$$

In a non-uniform finite-element mesh, as shown in Fig. A3, the spacing of the adjacent nodes on the left and right or above and below may differ. For such a finite element mesh, the finite difference method was used to calculate the derivatives, as shown in

$$\frac{\partial u_{i,j}}{\partial x} = \frac{\left(x_{i,j} - x_{i+1,j}\right) u_{i-1,j}}{\Delta x_{i-1} \left(\Delta x_i + \Delta x_{i-1}\right)} - \frac{\left(2x_{i,j} - x_{i-1,j} - x_{i+1,j}\right) u_{i,j}}{\Delta x_{i-1} \Delta x_i} + \frac{\left(x_{i,j} - x_{i-1,j}\right) u_{i+1,j}}{\Delta x_i \left(\Delta x_{i-1} + \Delta x_i\right)}, \tag{A17}$$

$$\frac{\partial u_{i,j}}{\partial y} = \frac{\left(y_{i,j} - y_{i,j+1}\right) u_{i,j-1}}{\Delta y_{i-1} \left(\Delta y_i + \Delta y_{i-1}\right)} - \frac{\left(2y_{i,j} - y_{i,j-1} - y_{i,j+1}\right) u_{i,j}}{\Delta y_{i-1} \Delta y_i} + \frac{\left(y_{i,j} - y_{i,j-1}\right) u_{i,j+1}}{\Delta y_i \left(\Delta y_{i,j-1} + \Delta y_{i,j}\right)}, \tag{A18}$$

$$\frac{\partial^2 u_{i,j}}{\partial x^2} = \frac{2u_{i-1,j}}{\Delta x_{i-1}\left(\Delta x_i + \Delta x_{i-1}\right)} - \frac{2u_{i,j}}{\Delta x_{i-1}\Delta x_i} + \frac{2u_{i+1,j}}{\Delta x_i\left(\Delta x_{i-1} + \Delta x_i\right)}, \tag{A19}$$

$$\frac{\partial^2 u_{i,j}}{\partial y^2} = \frac{2u_{i,j-1}}{\Delta y_{i-1}\left(\Delta y_i + \Delta y_{i-1}\right)} - \frac{2u_{i,j}}{\Delta y_{i-1}\Delta y_i} + \frac{2u_{i,j+1}}{\Delta y_i\left(\Delta y_{i-1} + \Delta y_i\right)}, \tag{A20}$$

where Δx_{i-1} is the spacing between nodes $(i-1,j)$ and (i,j), and Δx_i is the spacing between nodes (i,j) and $(i+1,j)$; Δy_{i-1} is the spacing between nodes $(i,j-1)$ and (i,j), and Δy_i is the spacing between nodes (i,j) and $(i,j+1)$.
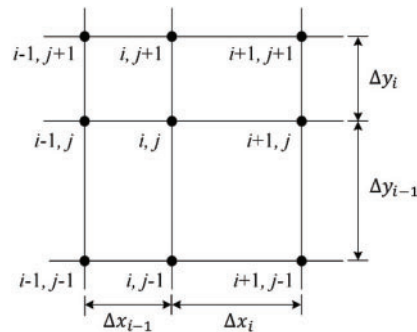
Figure A3: Non-uniform finite element mesh